Supplementary Information

Yuan Yuan[1], Gong Chen[1], Qihui Zhao[1], Yuanzun Fu[1], Yunhe Zhao[1, 2*]

[1] College of Chemistry, Chemical Engineering and Resource Utilization, Northeast Forestry University, 26 Hexing Road, Harbin, 150040, P.R. China.

[2] Center for Innovative Research in Synthetic Chemistry and Resource Utilization, Northeast Forestry University, Harbin 150040, P.R. China.

E-mail address: zhaoyunhe@nefu.edu.cn.

Experimental sections

Materials

All Chemicals were AR grade and obtained as follows: Cobalt nitrate hexahydrate ($Co(NO_3)_2 \cdot 6H_2O$), 2-methylimidazole ($C_4H_6N_2$) and hydrochloric acid (HCl, 28-30 wt%) were bought from Aladdin reagent (Shanghai, China). Potassium ferricyanide ($K_3[Fe(CN)_6]$) and potassium hydroxide (KOH) were supplied by Tianjin Chemical Reagent Co., Kay Tong. Ethanol was obtained from Tianjin Fuyu Fine Chemical Co., Ltd. They were ready for immediate use without further purification. Deionized (DI) water was used for cleaning up the surface residue of samples and preparing aqueous solutions throughout.

Preparation of Co MOF

Solution A was prepared by $Co(NO_3)_2 \cdot 6H_2O$ (2 mmol) was dissolved in 20 mL of DI water. Solution B was prepared by 2-methylimidazole (8 mmol) was dissolved in 20 mL DI water. Solution A was quickly poured into solution B and stirred. Then, the pretreated nickel foam (NF, 1 cm×1 cm) was immersed into the mixed solution and aged for 4 h at room temperature. Subsequently, the synthesized NF sheets were taken out, rinsed with DI water and dried at 60℃ overnight, denoted as Co MOF.

Preparation of Fe-doped Co MOF

$K_3[Fe(CN)_6]$ (0.658 g) was dissolved in 20 mL DI water, and then 20 mL of a mixed solution of ethanol and water ($V_{ethanol}$:V_{DI}=1:3) was added. Co MOF was immersed in the final mixed solution and aged for 12 h at room temperature. The obtained NF sheet was removed, rinsed several times with DI water and dried at 60℃ overnight, denoted as Fe-doped Co MOF.

Preparation of e-Fe-MOF CNs

Fe-doped Co MOF was immersed into 10 mL of 1 M HCl aged for 15 min, 30 min, and 60 min at room temperature. Finally, the HCl-etched NF nanosheets were obtained, removed, cleaned with DI water, and dried at 60℃ overnight, named as e-Fe-MOF CNs-15, e-Fe-MOF CNs-30 and e-Fe-MOF CNs-60, respectively.

Characterizations

Scanning electron microscope (SEM) were conducted with a JSM-7500F. Transmission electron microscopy (TEM), High-resolution transmission electron microscope (HRTEM), and the inset selected area electron diffraction (SAED) were taken on a JEM-2100. X-ray diffraction (XRD) analysis were performed on a TD-3500 using Cu-Ka radiation (l ¼ 0.154059 nm at 40 kV). Raman spectra data were acquired by a DXR2 20192805. Fourier transform infrared (FTIR) spectra data were taken on Nicolet iS 10. The X-ray photoelectron spectroscopy (XPS) data were collected by the surface analysis system (Thermofisher Escalab Xi+). Brunauer-Emmett-Teller (BET) surface area and pore size distribution with Nitrogen adsorption/desorption isotherms were measured using an Autosorb-iQ3 instrument by the Barrette Joynere Halenda (BJH) model. Ultraviolet-visible spectroscopy (UV-vis) data were obtained on a Cary100.

Electrochemical measurements

All electrochemical tests, including cyclic voltammetry (CV), constant current charge discharge (GCD), and electrochemical impedance spectroscopy (EIS), were conducted in 1 M KOH aqueous solution using a CHI 660E.

In the three-electrode system, the work electrode is the sample prepared at different etching time, and the platinum sheet and Hg/HgO electrode are used as the counter electrode and reference electrode, respectively. The CV curve was test under a potential window of 0-0.6 V at different scan rates of 2-50 mV s^{-1}. Within the potential window range of 0-0.5 V, GCD curves were obtained at different current densities of 1-20 A g^{-1}. The frequency range for EIS impedance testing is 0.01-10^5 Hz.

The specific capacity (C, C g^{-1}) of the electrode were calculated based on the GCD curves using the following formula:[1]

$$C = \frac{I\Delta t}{m} \tag{S1}$$

where I, Δt and m are the discharge current (A) and time (s) of the sample, and the sample quality (g).

In the two-electrode system, an asymmetric supercapacitor (ASC) is assembled using e-Fe-MOF CNs-30 as the positive electrode and AC as the negative electrode, with a cellulose separator between the positive and negative electrodes. AC electrode was obtained by mixing AC powder, koqin black, and 50 μL PVDF+NMP (weight ratio 8:1:1), perform ultrasound, and apply on the pre-treated 1 cm × 1 cm NF, dry and press. The loading capacity of positive and negative active substances is determined by the following equation:[2]

$$\frac{m_+}{m_-} = \frac{C_- \times \Delta V_-}{C_+ \times \Delta V_+} \tag{S2}$$

where m_+, C_+, ΔV_+ and m_-, C_-, ΔV_- are the mass (g), mass specific capacitance (mAh g^{-1}) and working potential windows (V) of positive and negative materials, respectively. In particular, the mass loading of e-Fe-MOF CNs-30 is 2 mg (2 mg cm^{-2}) and the AC loading is 4 mg. Similarly, the specific capacitance of the device is calculated based on the GCD curve using the following formula:[2]

$$C_{sc} = \frac{I \Delta t}{m \Delta V} \tag{S3}$$

where C_{sc} is the specific capacitance (F g^{-1}), I is the discharge current (A), Δt is the discharge time (s).

Moreover, the energy density and power density of the device could be calculated according to the formulas (S4) and (S5), as shown below:[3]

$$E = \frac{C_{sc} \Delta V^2}{2 \times 3.6} \tag{S4}$$

$$P = \frac{3600E}{\Delta t} \tag{S5}$$

where E is energy density (Wh kg^{-1}), C_{sc} is specific capacitance of the device (F g^{-1}), Δt is discharge time of the device (s), P is power density (W kg^{-1}).

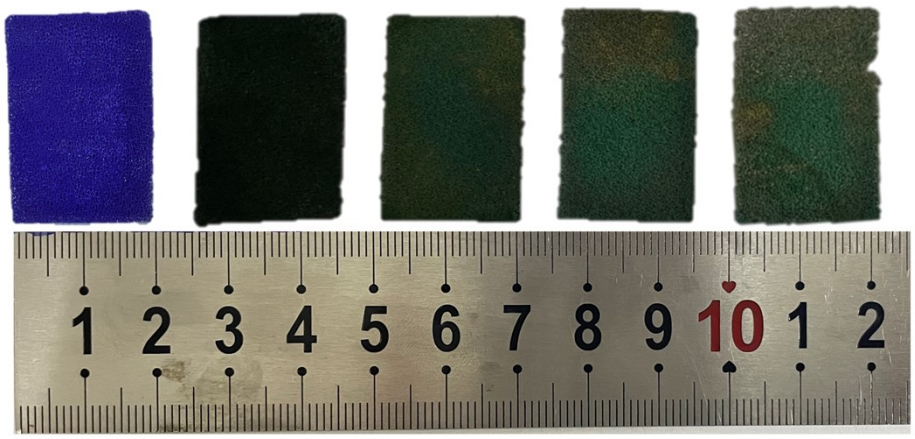

Fig. S1 The optical image of Co MOF, Fe-doped Co MOF, e-Fe-MOF CNs-15, e-Fe-MOF CNs-30 and e-Fe-MOF CNs-60 on NF.

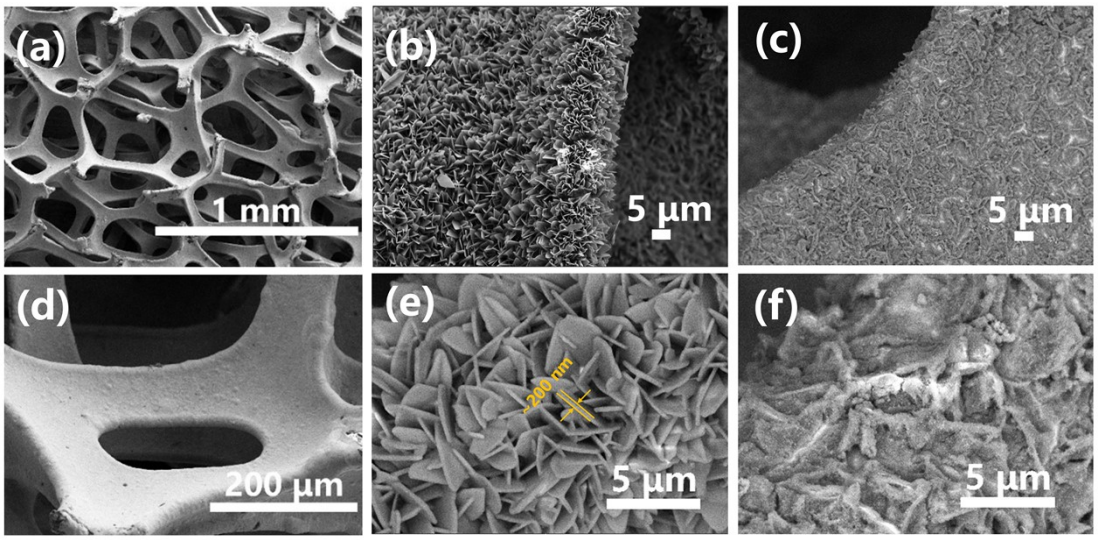

Fig. S2 SEM images. (a, d) NF, (b, e) Co MOF, (c, f) e-Fe-MOF CNs-30.

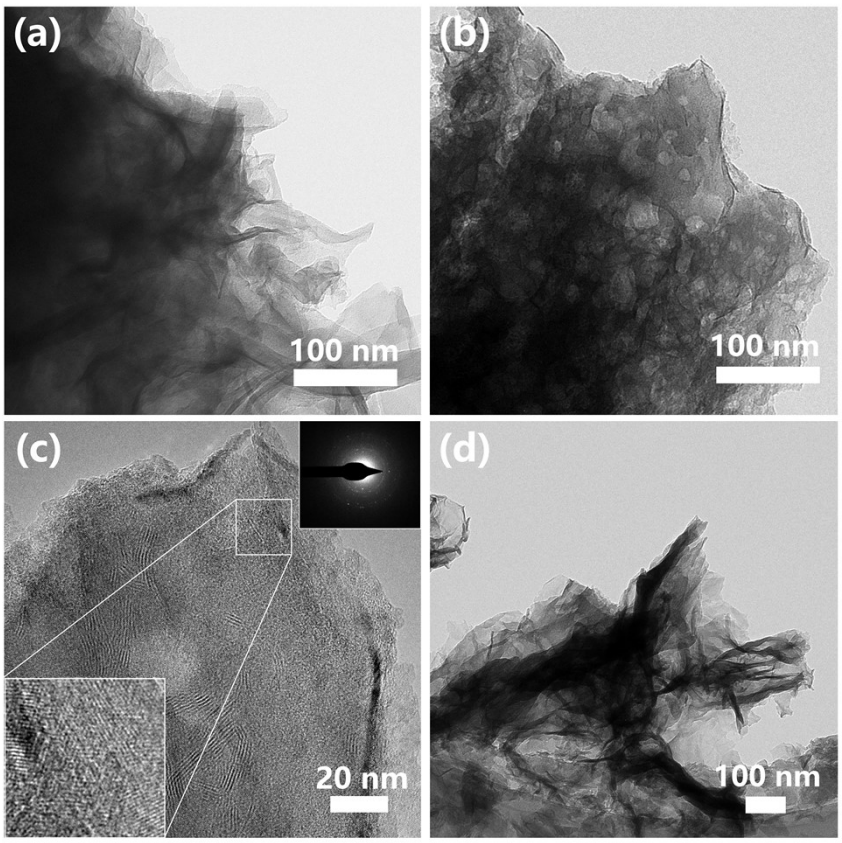

Fig. S3 Characterization data for e-Fe-MOF CNs. TEM image of (a) e-Fe-MOF CNs-15, (b) e-Fe-MOF CNs-30. (c) HRTEM image of e-Fe-MOF CNs-30 (Inset: SAED image). (d) TEM image of e-Fe-MOF CNs-60.

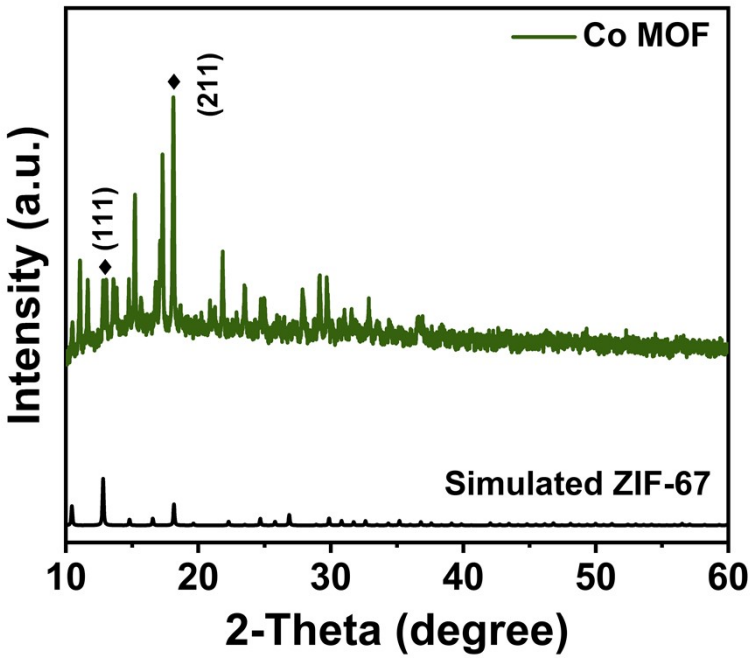

Fig. S4 XRD pattern for Co MOF.

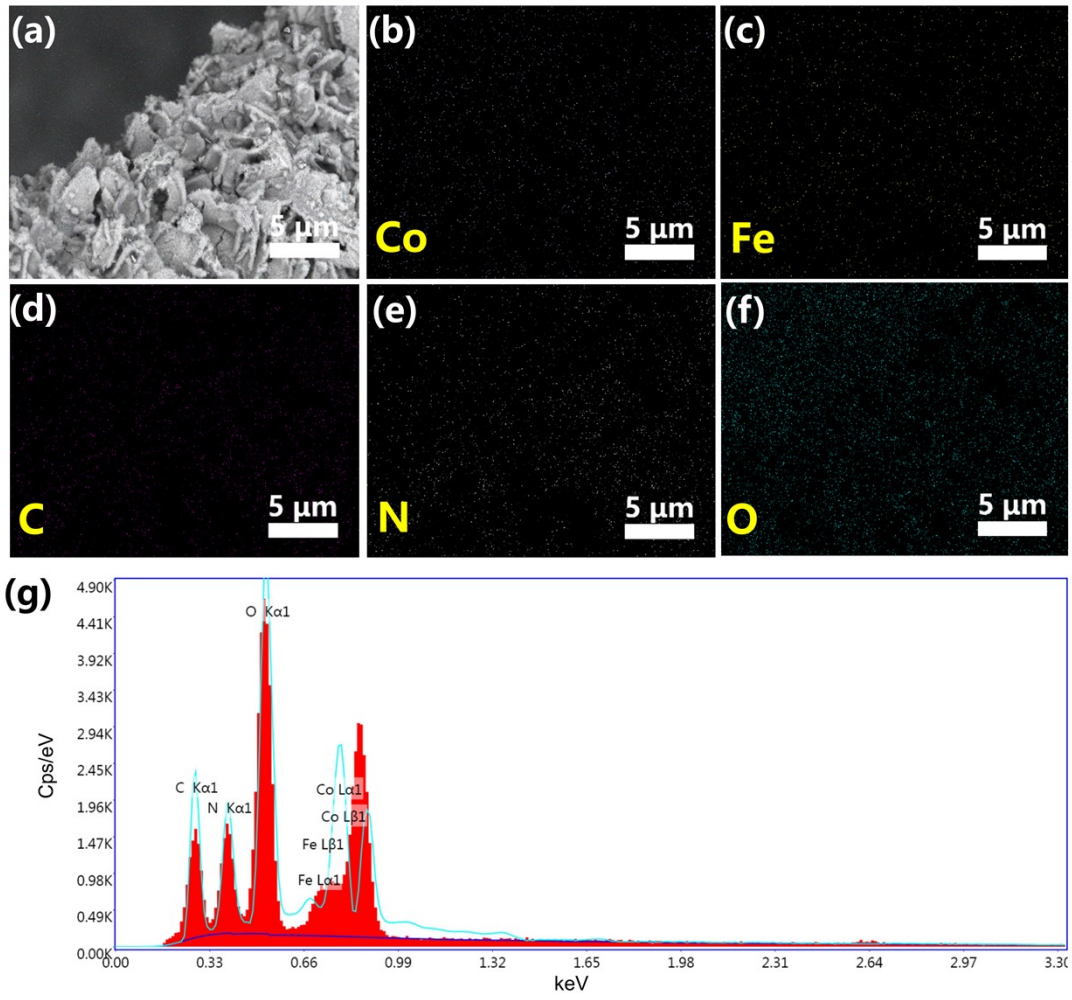

Fig. S5 Characterization data for e-Fe-MOF CNs-30. (a) SEM image. (b-f) Element mapping images for Co, Fe, C, N and O. (g) EDS spectrum.

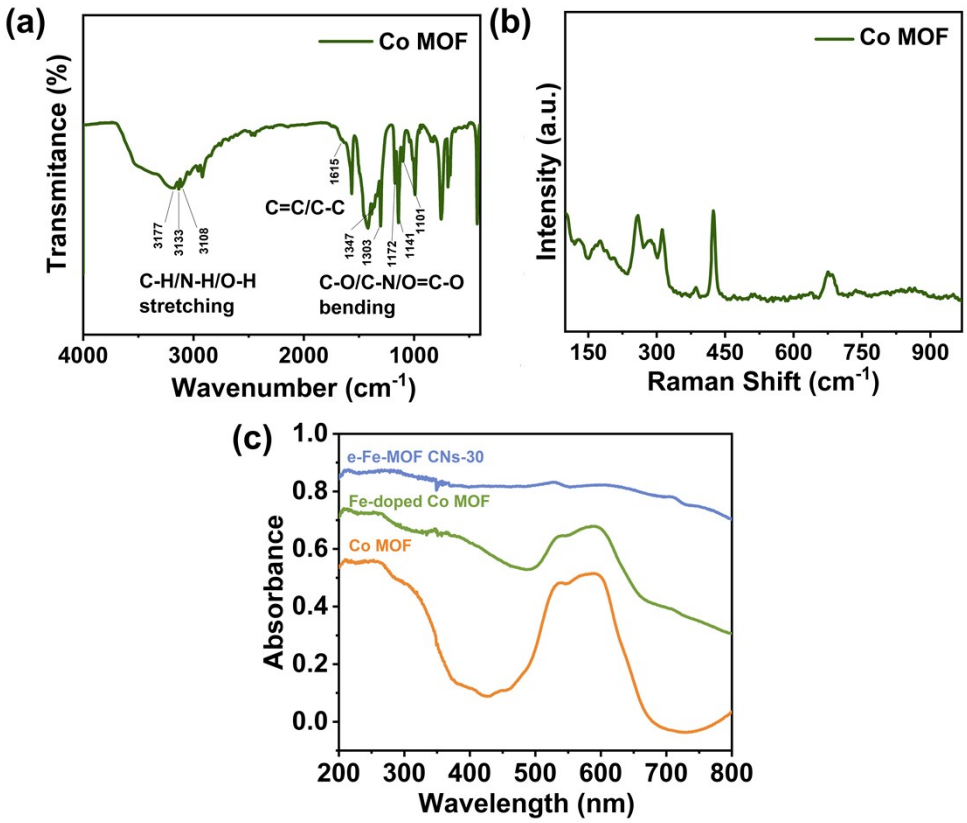

Fig. S6 Characterization data. (a) FTIR spectra. (b) Raman spectra. (c) UV-Vis spectra of Co MOF, Fe-doped Co MOF and e-Fe-MOF CNs-30.

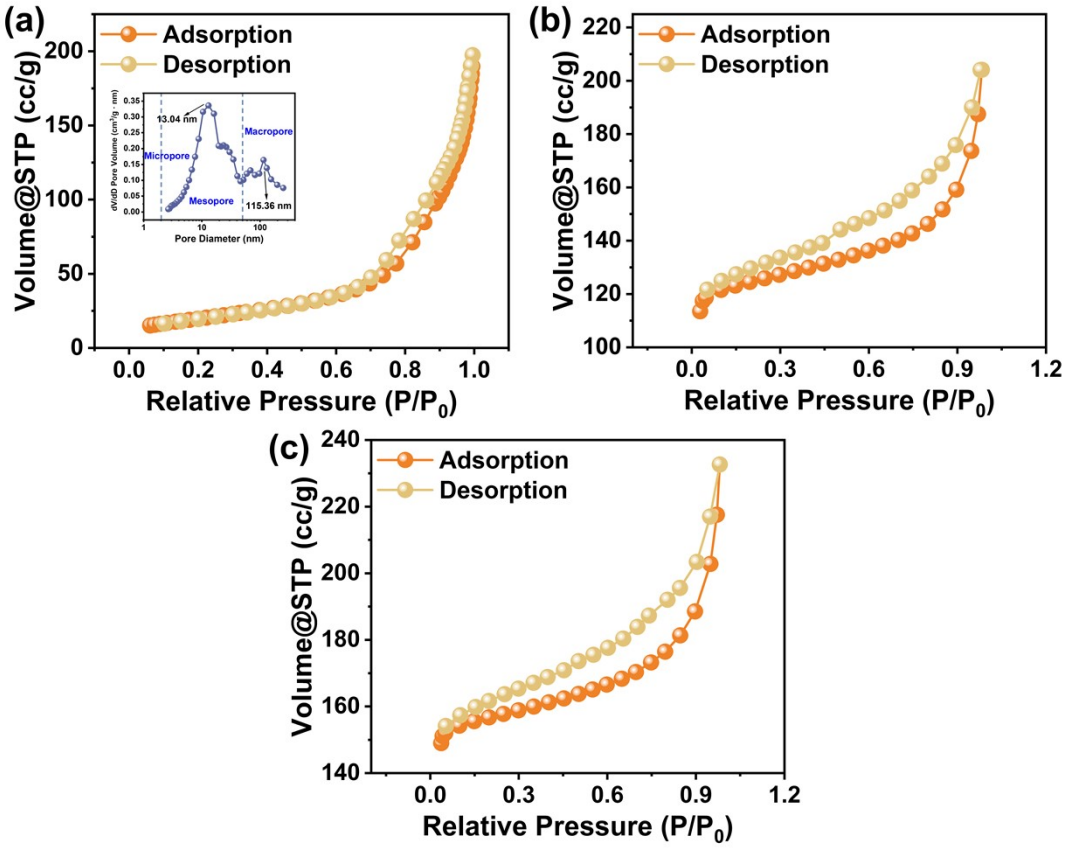

Fig. S7 N_2 adsorption-desorption isotherm curves. (a) Co MOF, (b) e-Fe-MOF CNs-15 and (c) e-Fe-MOF CNs-60.

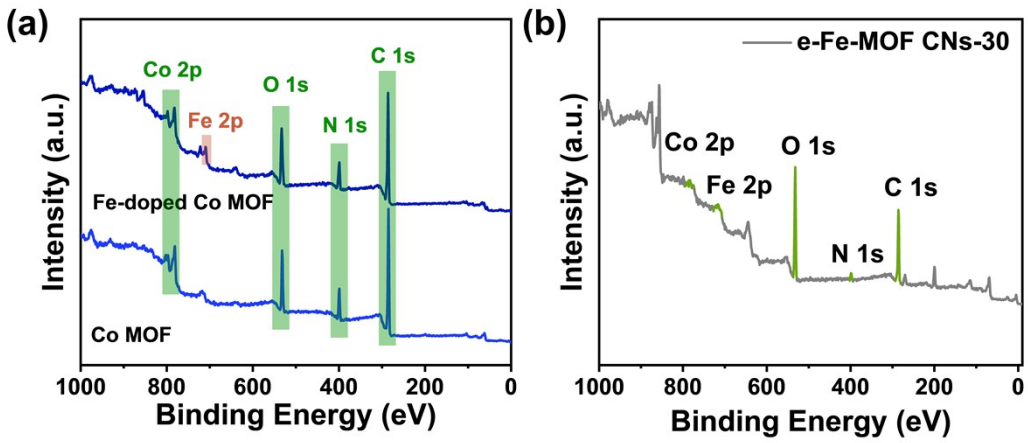

Fig. S8 XPS spectra of survey scan. (a) Co MOF, Fe-doped Co MOF, (b) e-Fe-MOF CNs-30.

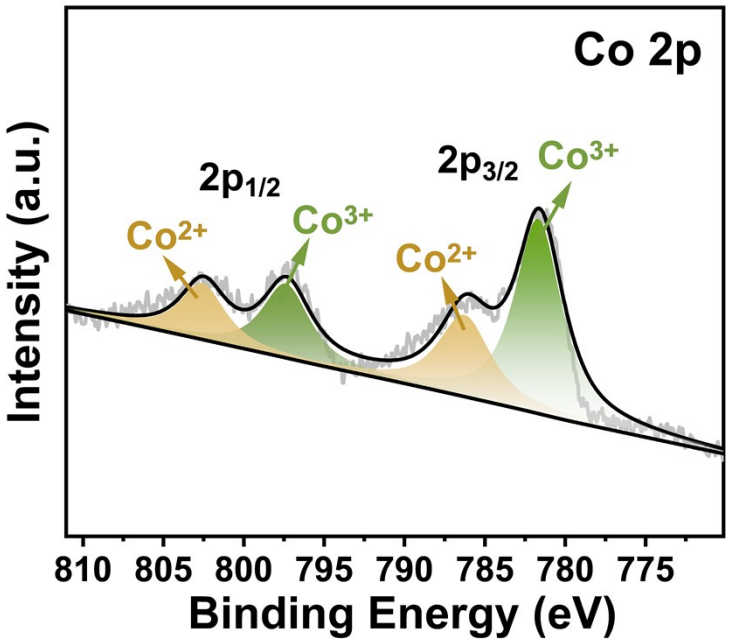

Fig. S9 XPS spectra of Co 2p in Co MOF.

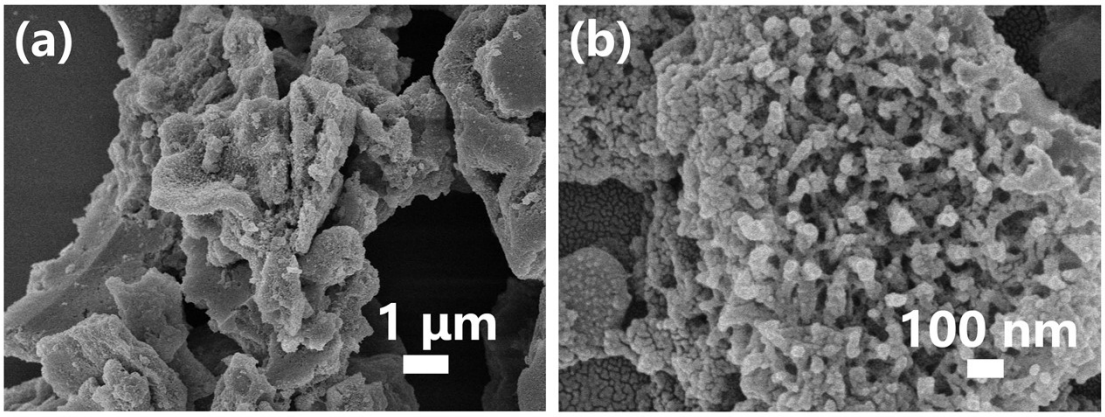

Fig. S10 SEM images of (a, b) Fe-doped Co MOF.

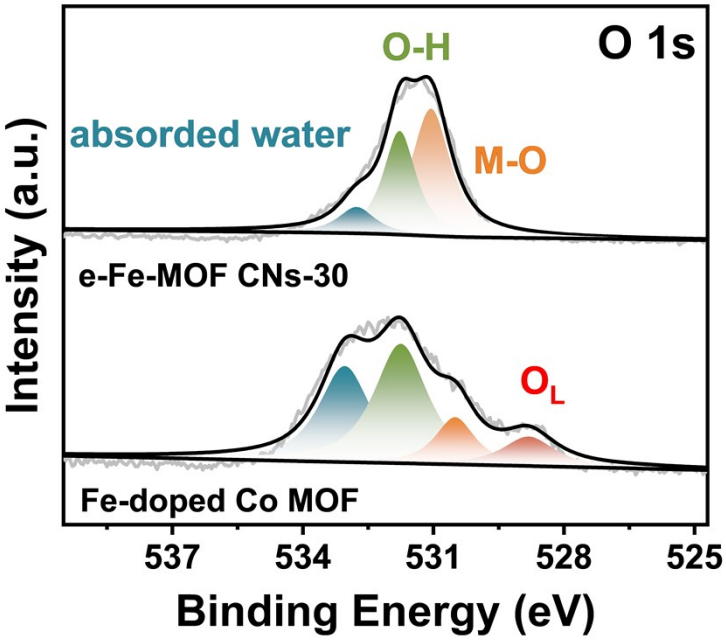

Fig. S11 XPS spectra of O 1s in Fe-doped Co MOF and e-Fe-MOF CNs-30.

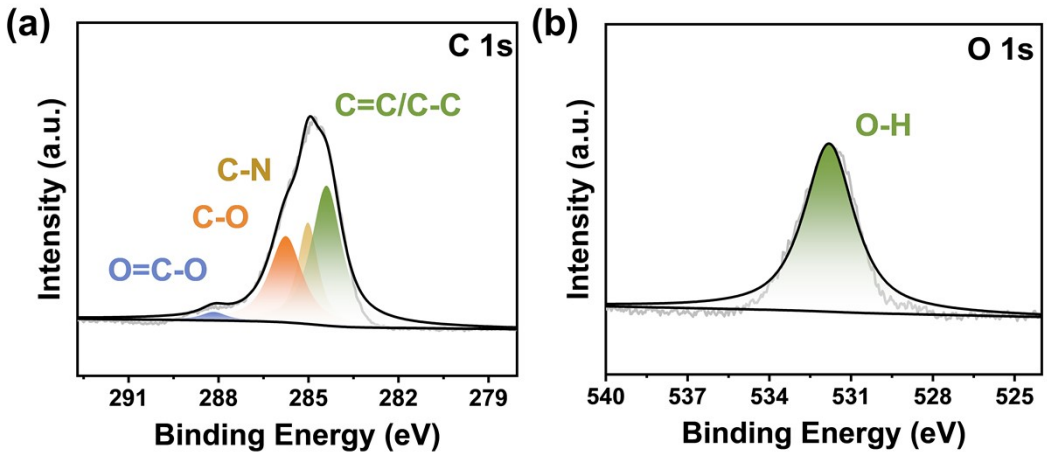

Fig. S12 XPS spectra of Co MOF. (a) C 1s, (b) O 1s.

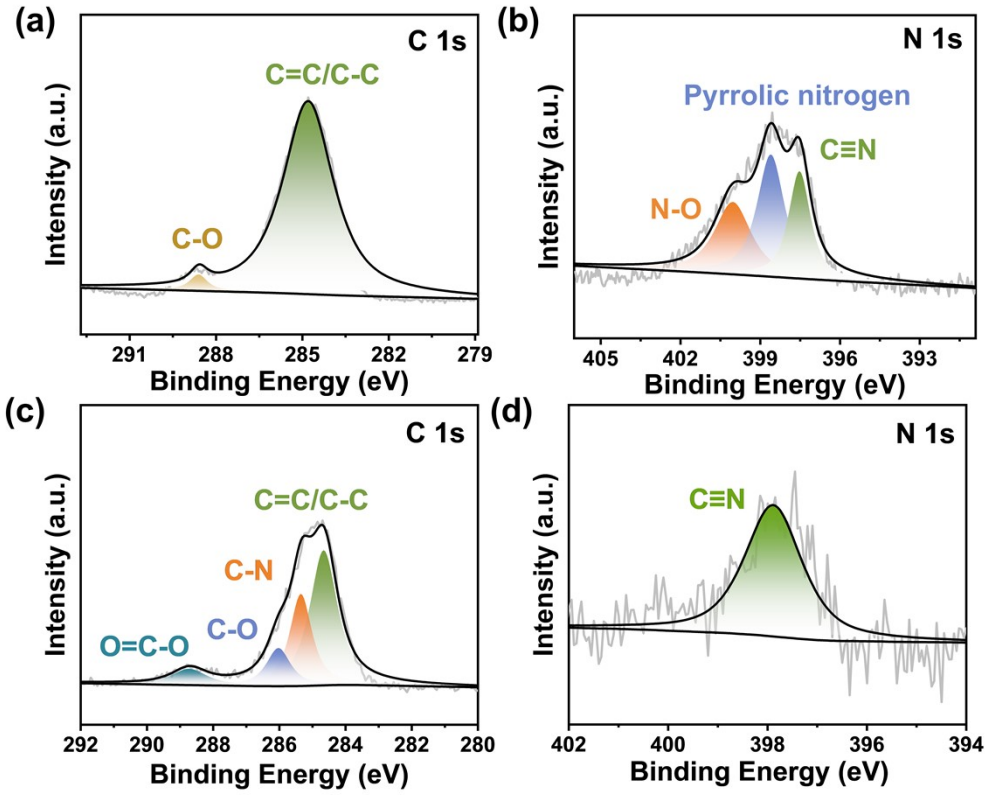

Fig. S13 XPS spectra of Fe-doped Co MOF and e-Fe-MOF CNs-30. (a, c) C 1s, (b, d) N 1s.

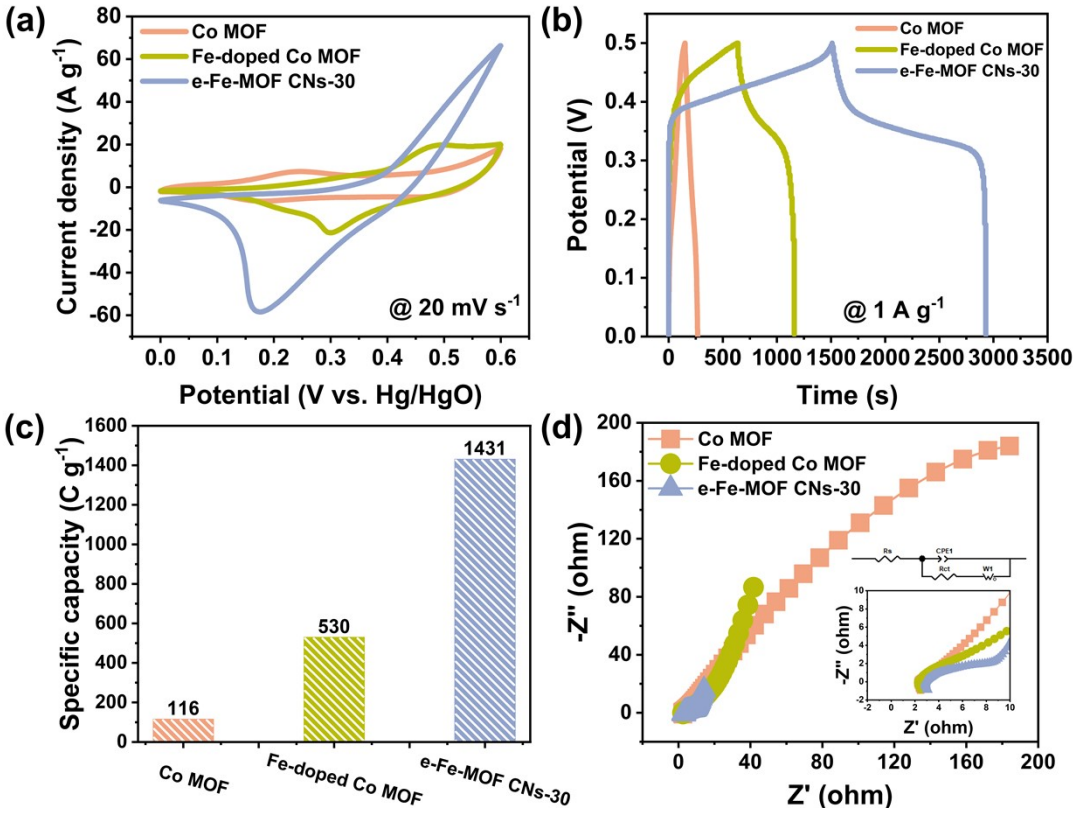

Fig. S14 Electrochemical performances of Co MOF, Fe-doped Co MOF and e-Fe-MOF CNs-30. (a) CV curves at 20 mV s^{-1}. (b) GCD curves at 1 A g^{-1}. (c) Specific capacity at 1 A g^{-1}. (d) Nyquist plots (Inset: magnified high-frequency region and circuit diagram).

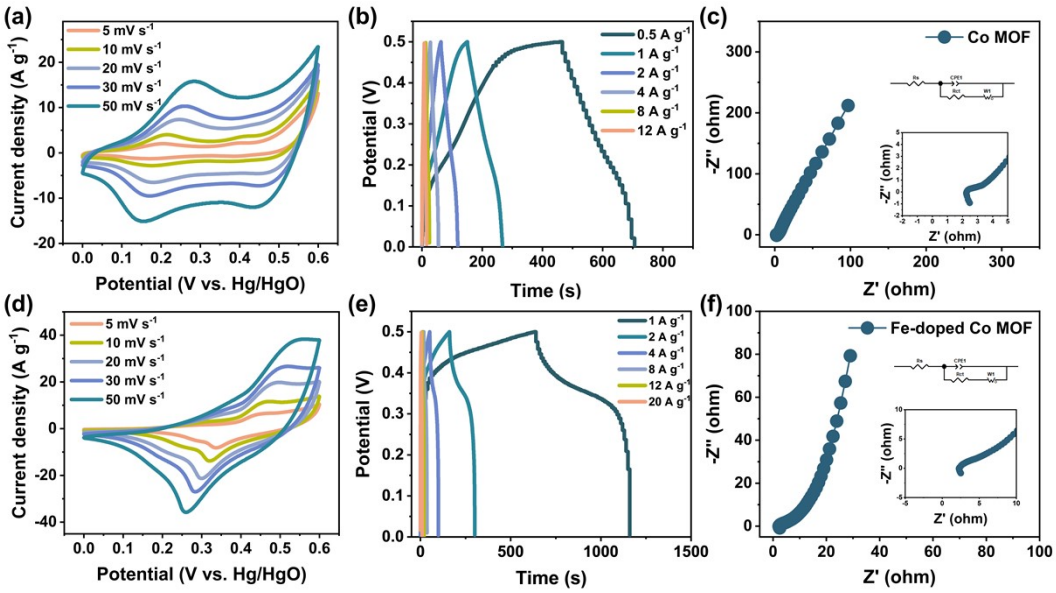

Fig. S15 Electrochemical performances of Co MOF, Fe-doped Co MOF. (a, d) CV curves at different scan rates. (b, e) GCD curves at different current densities. (c, f) Nyquist plots (Inset: magnified high-frequency region and circuit diagram).

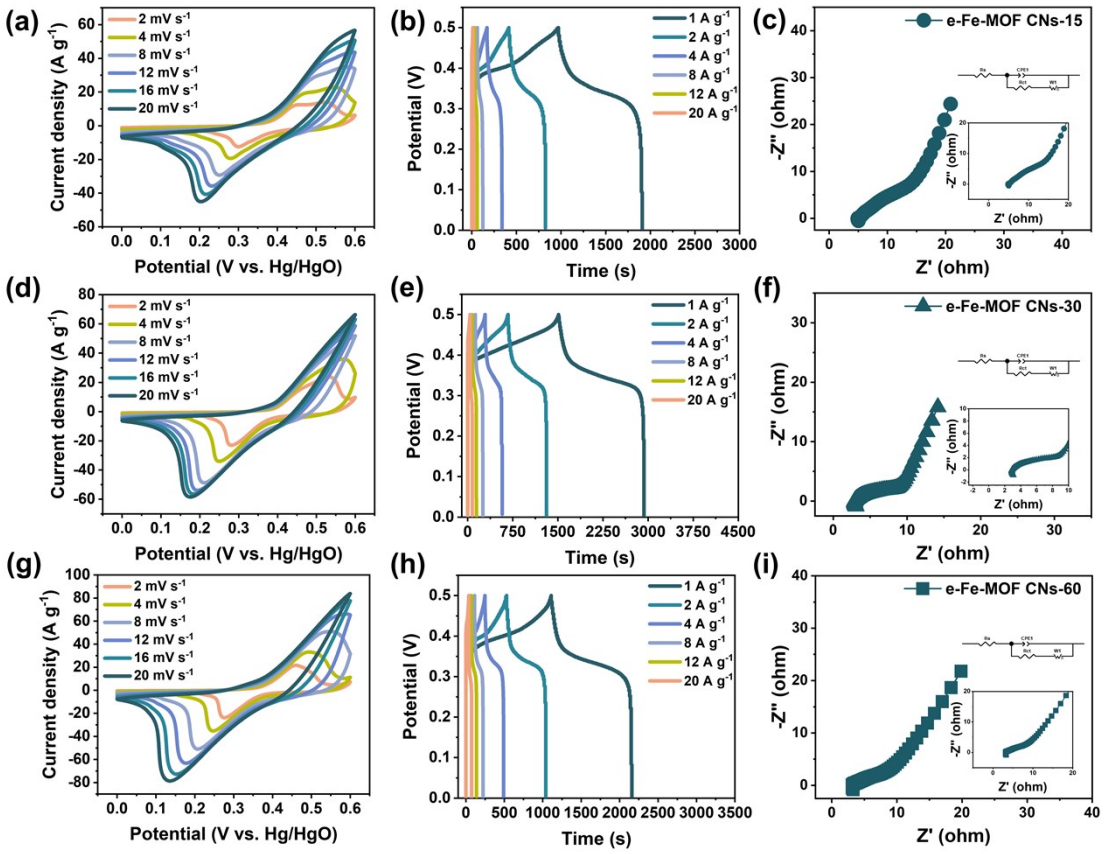

Fig. S16 Electrochemical performances of e-Fe-MOF CNs-15, e-Fe-MOF CNs-30 and e-Fe-MOF CNs-60. (a, d, g) CV curves at different scan rates. (b, e, h) GCD curves at different current densities. (c, f, i) Nyquist plots (Inset: magnified high-frequency region and circuit diagram).

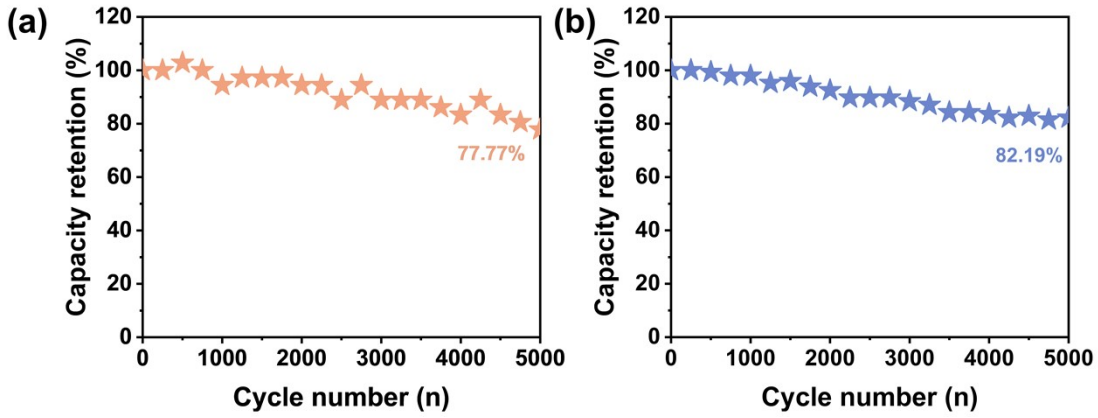

Fig. S17 The cyclic stability after 5000 charge-discharge cycles. (a) e-Fe-MOF CNs-15, (b) e-Fe-MOF CNs-60.

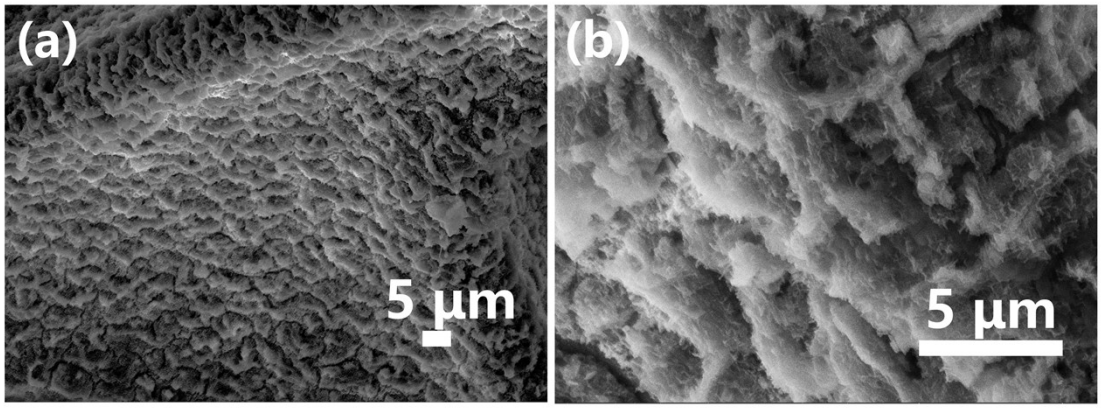

Fig. S18 SEM images of (a, b) e-Fe-MOF CNs-30 after 5000 charge-discharge cycles.

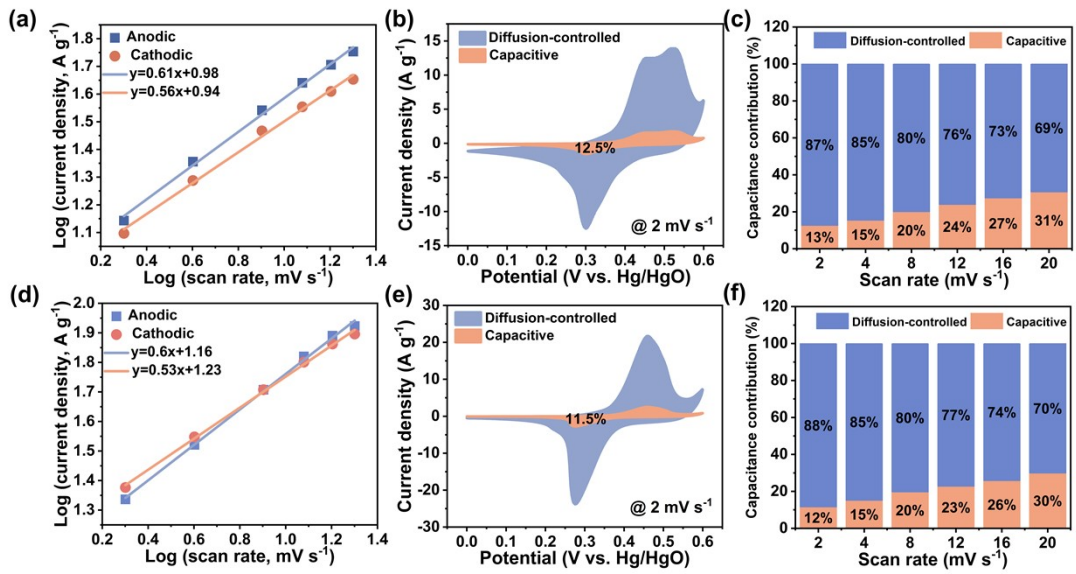

Fig. S19 Electrochemical performances of e-Fe-MOF CNs-15 and e-Fe-MOF CNs-60. (a, d) Linear relationships between log (*i*) and log (*v*). (b, e) The capacitive contribution at a scan rate of 2 mV s^{-1}. (c, f) Contribution ratios at various scan rates.

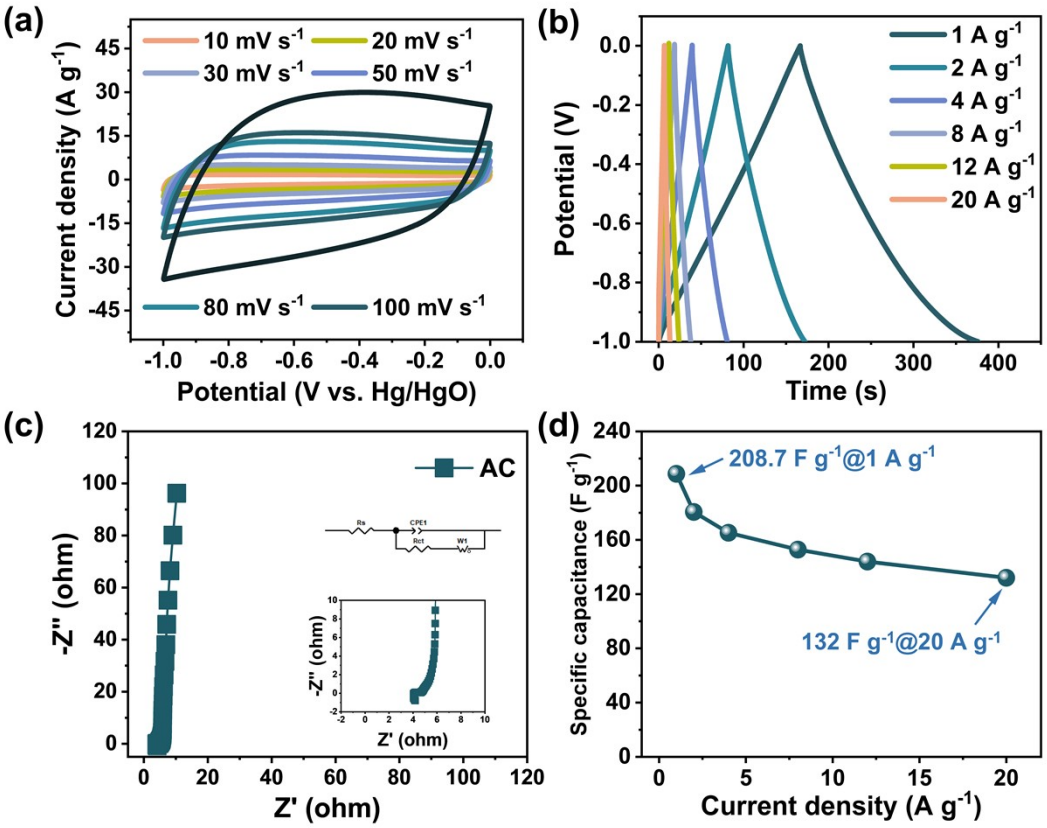

Fig. S20 Electrochemical performances of AC negative electrode. (a) CV curves at different scan rates. (b) GCD curves at different current densities. (c) Nyquist plots (Inset: magnified high-frequency region). (d) The specific capacitance at different current densities.

Table S1. Resistance values of e-Fe-MOF CNs-15, e-Fe-MOF CNs-30 and e-Fe-MOF CNs-60.

Electrode materials	R_s (Ω)	R_{ct} (Ω)
e-Fe-MOF CNs-15	5.024	9.486
e-Fe-MOF CNs-30	3.075	5.743
e-Fe-MOF CNs-60	3.298	5.848

Table. S2 Comparison of specific capacities in this work with other MOF-based electrodes.

Electrode materials	Methods	Electrolyte	Current density	Specific capacitance or capacity	Cyclic stability	Ref.
This work (e-Fe-MOF CNs-30)	**Coprecipitation**	**1 M KOH**	**1 A g^{-1}**	**1431 C g^{-1} /2862 F g^{-1}**	**84.2% after 5000 cycles**	
NiCo MOF	Ultrasonication	2 M KOH	1 A g^{-1}	1202.1 F g^{-1}	89.5% after 5000 cycles	4
NiCoP-MOF	Hydrothermal	2 M KOH	1 A g^{-1}	728 C g^{-1}	--	5
ZIF-67@PAIN	In-situ growth	1 M KOH	1 A g^{-1}	512 F g^{-1}	92.3% after 9000 cycles	6
Ni-MOF-2	Solvothermal	6 M KOH	1 A g^{-1}	467 C g^{-1}	83% after 5000 cycles	7
Zn-Co-MOF@CuO	Solvothermal	3 M KOH	2 A g^{-1}	684 F g^{-1}	111% after 10000 cycles	8
Ni/Co-MOF@TCT-NH_2	Solvothermal	3 M KOH	0.5 A g^{-1}	1924 F g^{-1}	58% after 10000 cycles	9
$Cu(NiCo)_2S_4/Ni_3S_4$	Hydrothermal	6 M KOH	1 A g^{-1}	1320 F g^{-1}	75% after 5000 cycles	10
$Ni_3S_4@Co_3S_4$	Sol-gel	1 M KOH	1 A g^{-1}	747.3 C g^{-1}	98.81% after 5000 cycles	11
ZnSCO-TAA@NiF	Coprecipitation	2 M KOH	10 mA cm^{-2}	743.7 C g^{-1}	81.6% after 15000 cycles	12
$CoNi_{0.5}$ MOF	Solvothermal	PVA/KOH	1 A g^{-1}	663.6 F g^{-1}	96% after 8000 cycles	13
MnCoNi-MOF	Hydrothermal	6 M KOH	1 A g^{-1}	655 F g^{-1}	92.3% after 10000 cycles	14
Mxene/CoS/NF	Coprecipitation	3 M KOH	2 mA cm^{-2}	0.91 mAh cm^{-2}	81.74% after 10000 cycles	15

Table. S3 Comparison of energy density and power density of e-Fe-MOF CNs-30//AC with other previously-reported devices.

Devices	Electrolyte	Voltage (V)	Energy density (Wh kg^{-1})	Power density (W kg^{-1})	Ref.
This work (e-Fe-MOF CNs-30//AC)	**1 M KOH**	**1.6**	**83.73**	**1600**	
Zn-Co MOF NS/rGO//3D rGO	6 M KOH	1.5	43	900	16
Ni_3S_4@Co_3S_4//AC	6 M KOH	1.4	30.7	388.5	17
Cu MOF/rGO//Cu-MOF/rGO	1 M Na_2SO_4	1.2	30.56	600	18
$CoNi_{0.5}$ MOF//N-doped graphene	PVA/KOH	1.6	23.44	350	13
Ni MOF@PPy//AC	2 M KOH+0.1 M $K_4Fe(CN)_6$	1.4	38.5	7001	19
MnCoNi MOF//AC	6 M KOH	1.6	61	844	14
MOF-B-600//AC	6 M KOH	1.6	63.62	400	20
NiCoP//AC	6 M KOH	1.5	36.87	2250	21
Ni MOF//AC	6 M KOH	1.6	30.4	407.4	22
Ni MOF-10//AC	2 M KOH	1.7	50.1	2550	23
CNHC-12h//AC	6 M KOH	1.6	41.8	800	24
NiCo-LDH-1//AC	1 M KOH	1.6	59.0	935.7	25
CuCN-MOF//CuCN-MOF	6 M KOH	1.2	68.175	5540	26
NiCo MOF//AC	2 M KOH	1.5	49.4	562.5	4
$SrCo_{0.95}Ta_{0.05}O_{3-\delta}$@CC//AC@CC	PVA/KOH	1.6	22.82	775.09	27
$SrCo_{0.95}Cr_{0.05}O_{3-\delta}$@CC//PPy@CC	3 M KOH	1.3	44.9	902.01	28

References

1 Y. Cao, N. Wu, C. Li, Y. Chen, H. Zhang, H. Guo and W. Yang, Solvent-regulated synthesis and phosphating of nickel-cobalt bimetal organic framework microflowers with hierarchical structure for high-performance supercapacitors, *Colloids and Surfaces A: Physicochemical and Engineering Aspects*, 2023, **658**, 130683.

2 J. Gao, T. Lian, Z. Liu and Y. He, 2D@3D MoS_2@Ni/Co-S submicroboxes derived from prussian blue analogues for high performance supercapacitors, *Journal of Alloys and Compounds*, 2022, **901**, 163558.

3 J. Jiang, Z. Li, X. He, Y. Hu, F. Li, P. Huang and C. Wang, Novel Skutterudite CoP_3-Based Asymmetric Supercapacitor with Super High Energy Density, *Small*, 2020, **16**, 2000180.

4 Y. Wang, Y. Liu, H. Wang, W. Liu, Y. Li, J. Zhang, H. Hou and J. Yang, Ultrathin NiCo-MOF Nanosheets for High-Performance Supercapacitor Electrodes, *ACS Applied Energy Materials*, 2019, **2**, 2063-2071.

5 S. He, F. Guo, Q. Yang, H. Mi, J. Li, N. Yang and J. Qiu, Design and Fabrication of Hierarchical NiCoP-MOF Heterostructure with Enhanced Pseudocapacitive Properties, *Small*, 2021, **17**, 2100353.

6 P. Liu, J. Zhao, Z. Dong, Z. Liu and Y. Wang, Interwoving polyaniline and a metal-organic framework grown in situ for enhanced supercapacitor behavior, *Journal of Alloys and Compounds*, 2021, **854**, 157181.

7 A. M. Kale, R. Manikandan, C. Justin Raj, A. Dennyson Savariraj, C. Voz and B. C. Kim, Protonated nickel 2-methylimidazole framework as an advanced electrode material for high-performance hybrid supercapacitor, *Materials Today Energy*, 2021, **21**, 100736.

8 I. Hussain, S. Iqbal, T. Hussain, W. L. Cheung, S. A. Khan, J. Zhou, M. Ahmad, S. A. Khan, C. Lamiel, M. Imran, A. AlFantazi and K. Zhang, Zn-Co-MOF on solution-free CuO nanowires for flexible hybrid energy storage devices, *Materials Today Physics*, 2022, **23**, 100655.

9 L. Yue, L. Chen, X. Wang, D. Lu, W. Zhou, D. Shen, Q. Yang, S. Xiao and Y. Li, Ni/Co-MOF@aminated MXene hierarchical electrodes for high-stability supercapacitors, *Chemical Engineering Journal*, 2023, **451**, 138687.

10 W. Zhao, G. Yan, Y. Zheng, B. Liu, D. Jia, T. Liu, L. Cui, R. Zheng, D. Wei and J. Liu,

Bimetal-organic framework derived $Cu(NiCo)_2S_4/Ni_3S_4$ electrode material with hierarchical hollow heterostructure for high performance energy storage, *Journal of Colloid and Interface Science*, 2020, **565**, 295-304.

11 F. Hadji, M. Omari, M. Mebarki, N. Gabouze and A. Layadi, Zinc doping effect on the structural and electrochemical properties of $LaCoO_3$ perovskite as a material for hybrid supercapacitor electrodes, *Journal of Alloys and Compounds*, 2023, **942**, 169047.

12 R. Balamurugan and A. C. Bose, Surface-sulfurized Zn-MOF Grown on Ni-foam with Various Sulfurizing Agents for Aqueous Hybrid Super capacitor Device Fabrication, *ACS Applied Energy Materials*, 2024, **7**, 974-985.

13 W. Zhang, X. Guo, Y. Wang, Y. Zheng, J. Zhao, H. Xie, Z. Zhang and Y. Zhao, Self-Assembly of Ni-Doped Co-MOF Spherical Shell Electrode for a High-Performance Supercapacitor, *Energy & Fuels*, 2022, **36**, 1716-1725.

14 X. Han, P. Wang, Y. Zhang, H. Liu, J. Tang, G. Yang and F. Shi, Addition of dissimilar metal nodes to improve the electrochemical performance of MOF as a supercapacitor, *Inorganica Chimica Acta*, 2022, **536**, 120916.

15 X. Liang, Y. Chen, Z. Jiao, M. Demir, M. Du and J. Han, MXene-transition metal sulfide composite electrodes for supercapacitors: Synthesis and electrochemical characterization, *Journal of Energy Storage*, 2024, **88**, 111634.

16 H. Wu, S. Li, Y. Liu and Y. Shi, Self-assembled Zn-Co MOF nanospheres/rGO as cathode material for an asymmetric supercapacitor with high energy density, *Electrochimica Acta*, 2023, **462**, 142740.

17 J. Xu, H. Guo, M. Wang, Y. Hao, J. Tian, H. Ren, Y. Liu, B. Ren and W. Yang, Hollow $Ni_3S_4@Co_3S_4$ with core-satellite nanostructure derived from Metal-organic framework (MOF)-on-MOF hybrids as electrode material for supercapacitor, *Dalton Transactions*, 2024, **53**, 4479-4491.

18 S. Krishnan, A. K. Gupta, M. K. Singh, N. Guha and D. K. Rai, Nitrogen-rich Cu-MOF decorated on reduced graphene oxide nanosheets for hybrid supercapacitor applications with enhanced cycling stability, *Chemical Engineering Journal*, 2022, **435**, 135042.

19 Z. Qin, Y. Xu, L. Liu, M. Liu, H. Zhou, L. Xiao, Y. Cao and C. Chen, Ni-MOF composite polypyrrole applied to supercapacitor energy storage, *RSC Advances*, 2022, **12**, 29177-

29186.

20 D. Huang, L. Chen, L. Yue, F. Yang, H. Guo and W. Yang, Nitrogen-doped carbon-enriched MOF and derived hierarchical carbons as electrode for excellent asymmetric aqueous supercapacitor, *Journal of Alloys and Compounds*, 2021, **867**, 158764.

21 S. Kavian, S. Hajati and M. Moradi, High-rate supercapacitor based on NiCo-MOF-derived porous NiCoP for efficient energy storage, *Journal of Materials Science: Materials in Electronics*, 2021, **32**, 13117-13128.

22 J. Wang, Y. Ma, X. Kang, H. Yang, B. Liu, S. Li, X. Zhang and F. Ran, A novel moss-like 3D Ni-MOF for high performance supercapacitor electrode material, *Journal of Solid State Chemistry*, 2022, **309**, 122994.

23 Y. Pan, Y. Han, Y. Chen, D. Li, Z. Tian, L. Guo and Y. Wang, Benzoic acid-modified 2D Ni-MOF for high-performance supercapacitors, *Electrochimica Acta*, 2022, **403**, 139679.

24 X. Jia, Y. Zhao, X. Xu, Z. Xiao, S. Lv, F. Zhou, Q. Zhang, C. Chen, J. Liu and L. Wang, Construction of Double-Shell Basic Cobalt/Nickel Carbonate Microspheres via MOFs Etching Strategy for Boosting Aqueous Supercapacitor Performances, *ACS Applied Energy Materials*, 2023, **6**, 9108-9117.

25 H. Jiang, Q. Ke, X. Qiu, J. Chen, P. Chen, S. Wang, X. Luo and B. Rao, NiCo layered double hydroxide nanocages for high-performance asymmetric supercapacitors, *Inorganic Chemistry Frontiers*, 2023, **10**, 2154-2164.

26 S. Mishra, M. K. Singh, D. Pandey, D. K. Rai and A. Raghuvanshi, A two-dimensional semiconducting Cu(i)-MOF for binder and conductive additive-free supercapattery, *Journal of Materials Chemistry A*, 2024, **12**, 4535-4543.

27 G. Liu, L. Liu, G. Li, S. Wu, J. He, Y. Zhou, M. Demir and P. Ma, Temperature-Dependent Electrochemical Performance of Ta-Substituted $SrCoO_3$ Perovskite for Supercapacitors, *Chemistry-A European Journal*, 2024, **30**, e202303267.

28 J. He, Y. Zhou, S. Wu, L. Jin, J. Cao, M. Demir and P. Ma, Cr-Substituted $SrCoO_{3-\delta}$ Perovskite with Abundant Oxygen Vacancies for High-Energy and Durable Low-Temperature Antifreezing Flexible Supercapacitor, *Inorganic Chemistry*, 2024, **63**, 13755-13765.